Flow Field Measurements to Characterize Flap Side-Edge Noise Generation

Karl-Stéphane Rossignol*

German Aerospace Center (DLR), Lilienthalplatz 7, 38108 D-Braunschweig

In this paper, the relation between noise generated at flap side-edges (FSE) and mean flow characteristics in the vicinity of the FSE solid surface is investigated. Of interest is (1) the identification of mean flow features near the flap tip which are important to FSE noise generation, (2) the extraction of quantitative parameters relating flap settings to the emitted noise levels and, finally, (3) the formulation of a prediction scheme based on these observations. The results of the investigation demonstrate that FSE noise can be properly represented by the summed contributions of two independent source mechanisms. Moreover, this new formulation necessitates only a limited knowledge of the mean flow parameters in the vicinity of the FSE to model the noise emission. It is assumed that unsteady vorticity fluctuations, originating from the unstable pressure side shear layer, sweeping over the forward half of the upper tip edge, lead to mid-to-high frequency noise production. Flow unsteadiness in the proximity of the suction side surface near the FSE aft half, are assumed to be the main contributor in the low-to-mid frequency range. A prediction scheme is formulated and validated for a wide range of experimental measurements at small scale wing configurations. This new formulation only necessitates knowledge of the flap chord length and lift coefficient to provide accurate estimates of the far field noise radiation.

Nomenclature

α	Aircraft angle of attack [°]
δ_F	Geometric flap deployment angle [°]
δ'_F	Effective flap deployment angle [°]
κ_0	Helmholtz number [-]
$\mu_{0,1,2}$	Spectral shape function constants [-]
ν	Kinematic viscosity [m^2/s]
Π	Far field noise power spectral density [p^2/Hz]
ρ	Density of air [kg/m^3]
σ	Wing sweep angle [°]
φ_x	Polar emission angle [°]
φ_y	Azimuthal emission angle [°]
A_g	Geometry-related noise amplitude [dB]
c	Profile chord length [m]
c_0	Speed of sound in air [m/s]
C_L	Lift coefficient ($= F_N/0.5\rho U_0^2 S$)[-]
d	Profile maximum thickness [m]
f	frequency [Hz]
F_N	Lift force [N]
$f_{1/3}$	1/3-octave band central frequency [Hz]
I	Sound intensity [W/m^2]
L	Characteristic geometric length scale [m]
l_0	Characteristic length scale of turbulence [m]
$l_{1,2,3}$	Flow coherence length scale [m]
$L_{p,1/3}$	1/3-octave band sound pressure level [dB]

*Research Engineer, Technical Acoustics Department, Institute of Aerodynamics and Flow Technology, karl-stephane.rossignol@dlr.de

M_0	Mach number based on the free-stream velocity ($= U_0/c_0$) [-]
M_c	Mach number based on the PS cross-flow velocity ($= U_c/c_0$) [-]
M_{loc}	Local Mach number ($= U/c_0$) [-]
Re	Reynolds number ($= U_0 c/\nu$) [-]
s	Profile span [m]
St_0	Strouhal number based on the free-stream velocity ($= fL/U_0$) [-]
St_{loc}	Local Strouhal number ($= fl_0/U$) [-]
T	Characteristic time scale [s]
U	Characteristic velocity scale [m/s]
U_0	Mean free-stream velocity [m/s]
u_0	Characteristic velocity scale of turbulence [m/s]
U_1	Mean streamwise velocity [m/s]
U_2	Mean spanwise velocity [m/s]
U_3	Mean normal velocity [m/s]
U_c	Maximum spanwise velocity magnitude at the lower tip edge [m/s]
W	Functional dependency on Mach number
x, y, z	Streamwise, spanwise and normal wind tunnel coordinates [m]
x_1, x_2, x_3	Streamwise, spanwise and normal source coordinates ($\mathbf{x} = \{x_1, x_2, x_3\}$) [m]
y_1, y_2, y_3	Streamwise, spanwise and normal field coordinates ($\mathbf{y} = \{y_1, y_2, y_3\}$) [m]

I. Introduction

THE quest toward the development of the next-generation environmentally friendly aircraft imposes stringent restrictions on noise emissions. This calls for new ideas and innovative technologies for the US and European noise reduction targets to be met. New designs and novel configurations might lead to the occurence of new dominant sources of sound and new effects could gain in importance, e.g. interaction between components or sound shielding. Also, changes in noise source ranking can occur. Current semi-empirical airframe noise prediction schemes cannot accurately evaluate noise emission from such unconventional aircraft. The demand for precise airframe noise level estimation at low computational costs will therefore remain important. Requiring prediction schemes to become more fine-grained. One avenue is to represent noise sources by integrating more of the flow physics in their modelling. This approach will be favored in this paper. Our attention is turned to a single known noise contributor of the high-lift system, namely, the flap side-edge (FSE).

Because of the complexity of the flow dynamics driving FSE noise generation, an analytical solution to Lighthill's analogy is not available. Analytical work is therefore limited to simplified cases which do not arise in reality but are still pertinent enough to reveal dominant factors responsible for the noise production.[1–4] Computational aeroacoustics (CAA) is also an interesting avenue which can provide much insight into a problem. It is, however, too costly for aircraft design studies and optimization. This is where semi-empirical source representations are of great interest. Such models are mostly derived from experimental data using regression analysis.[5–7] Their inherent limitations are twofold, **(1)** no physical meaning of the regression parameters and **(2)** a limited range of validity because these methods are calibrated on specific databases. A deeper look into the flow physics is first necessary to overcome these difficulties and provide a better understanding of the source mechanisms.

Aerodynamic noise generation at the FSE is due to the formation of a double-vortex structure at the flap tip, and its interaction with the component surfaces during the process. The vortices are formed by the rapid roll-up of the suction side (SS) and pressure side (PS) shear layers shed off the tip edges. One vortex develops on the SS and a second one on the tip face. The SS and tip vortices grow continuously with streamwise position, fed by the PS shear layer, and eventually merge to a single larger vortical structure around mid-chord, where the tip vortex moves to the SS. At low deflection angles this vortex system remains near the flap surface, evetually reaching the tip's trailing-edge (TE). Large flap deflections lead to an earlier lift-off of the merged vortex from the SS.

Two different mechanisms responsible for FSE noise are described in the literature, **(1)** shear layer unsteadiness and **(2)** vortex unsteadiness interacting with the FSE surfaces and edges. The first mechanism refers explicitly to unsteady shear layers shed at the SS and PS sharp edges in the forward half of the model (see locations 1 and 2 in figure 1). The initial underlying characteristic wavelength of the unsteady shear layer is of the order of the PS boundary layer thickness[8] (i.e.$\ll d$). A stability analysis made by Streett[9] as well as wind tunnel measurements made at NASA[10] suggest that the shear layer instability mechanism should contribute to the mid-to-high frequency part of the FSE noise spectrum. Although the flow at the tip edges is subjected to rapid distortions, the magnitude of the unsteadiness in their im-

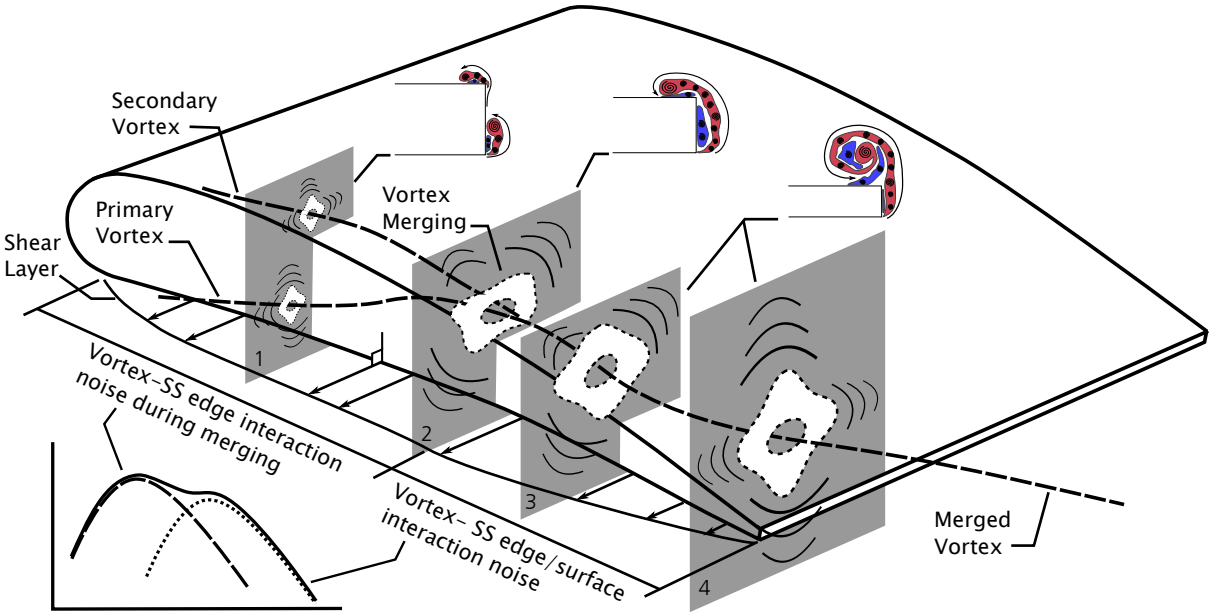

Figure 1: Simplified representation of the mechanisms of FSE noise production. The section cuts show snapshots of the vorticity field near the FSE (Blue: negative vorticity, Red: positive vorticity). The vortex path is shown by the dashed line. Mid-to-high frequency vortex-edge interaction noise occur mostly at location 1 and 2. At locations 3 and 4, Low-to-mid frequency noise production due to vortex-edge, -surface interactions. A schematic view of the spectra of FSE noise and its two main contributors is provided at the bottom left corner.

mediate vicinity is small because the shear layer development is at an early stage. It is therefore unlikely that this mechanism alone is an important contributor to the total emitted noise. This is supported by unsteady pressure measurements near the flap edges which show levels an order of magnitude lower over the whole frequency range on the PS relative to SS levels.[11–13] Correlation analysis between surface sensors also indicate a dominant source of noise near the SS edge, underneath the path of the vortex.[12] More probable is therefore a combined contribution from a pure shear layer instability mechanism at the PS and SS edge and the interaction of the resulting unsteady velocity/vorticity fluctuations with the tip SS edge during vortex merging. The second mechanism is related to vortex-structure interactions in the aft half of the model chord in the vicinity of the flap tip upper edge (see locations 3 and 4 in figure 1). It is an efficient radiator in the mid- to long-wavelength range.[9,10,12] Storms[13] refers to this mechanism as "vortex scrubbing". These observations provide a basis for the development of an empirical prediction model for FSE noise. To the author's knowledge, the recent work of Guo[14] is the only attempt to model FSE noise according to the above observations.

Guo's model was used to represent experimental data covering a wide range of configurations, raising questions about an appropriate choice for the characteristic velocity and length scales. The purpose of this study is therefore to investigate the relationship between the model's parameters and the physics responsible for FSE noise generation. This is accomplished by detailed measurements of the FSE flow field in the vicinity of the tip edges to identify characteristics flow features which are related to the mechanisms discussed above. Characteristic parameters will be quantified and used in conjunction with Guo's empirical model to achieve a very good representation of the experimental data.

II. Theory

In this section an overview of Guo's model for the spectral shape of FSE noise is given. Only the main conclusions are discussed. For further details, the reader is referred to Guo 2011.[14]

Noise generation from aircraft flaps is commonly assumed to be due to surface pressure fluctuations and, therefore, to be mainly related to the dipole source of the solution to the Ffowcs Williams & Hawkings wave equation. A general form for this term is,

$$\Pi(\mathbf{x},\omega) = \int_{S(\mathbf{y})} \Pi_0(\mathbf{y})\Phi_1(\kappa_1)\Phi_2(\kappa_2) l_1 l_2 \tau_0 \Psi(\omega) \left| n_i(\mathbf{y}) \frac{\partial G_0(\mathbf{x}-y)}{\partial y_i} \right|^2 dS(\mathbf{y}). \tag{1}$$

where dS defines a surface element for the integration. According to Guo,[14] three main contributors to the spectral shape of FSE noise can be identified. Namely, the Green's function (G_0) and its gradients as well as the temporal and spatial coherences of the source. The derivatives of Green's function are proportional to the acoustic wavenumber,

$$\left|\frac{\partial G_0}{\partial y_i}\right|^2 \sim f^2 \left|G_0(f)\right|^2 \rightarrow \kappa_0^2 = \left(\frac{fl}{c_0}\right)^2, \tag{2}$$

where $\kappa_0 = fl/c_0$ is the Helmholtz number. The temporal coherence of the FSE noise source is related to the most energetic flow structures existing in the vicinity of the flap tip. These flow characteristics are assumed to dominate the noise production and their time scale is determined by their characteristic turbulent length (l_0) and velocity scales (u_0),

$$T \approx \frac{l_0}{u_0} = \mu_0 \frac{L}{U}, \tag{3}$$

where U is a relevant characteristic mean flow velocity scale and L a characteristic geometric scale of the problem considered. The corresponding peak frequency estimate is therefore $f = T^{-1}$Hz and the Strouhal number of the dominant structures is, per definition, equal to unity. The equal sign in equation 3 expresses the proportionality between the locally dominant flow structures scales and relevant geometrical and mean flow characteristics. The final result for the temporal coherence of the source is

$$\Psi(f) = \frac{1}{1 + \mu_0^2 St_0^2}. \tag{4}$$

For the source spatial coherence Guo provides the following two results for the streamwise and spanwise directions, respectively:

$$\Phi_1(f) = \frac{1}{1 + \mu_1^2 (1 + M_0)^2 St_0^2}, \tag{5}$$

$$\Phi_2(f) = \frac{1}{1 + \mu_2^2 (\kappa_0)^2}. \tag{6}$$

Guo argues that, for both $\Phi_1(f)$ and $\Phi_2(f)$, the coherence length should scale on L,

$$l_1 = \mu_1 L \text{ and } l_2 = \mu_2 L \text{ with } L = c \text{ or } d. \tag{7}$$

The constants μ_0, μ_1 and μ_2 in equations 4 to 6 are all of order unity. A model for the spectral shape (F_0) of FSE noise is finally obtained by collecting the results of equations 2, 4, 5 and 6. One gets the form function,

$$F_0 = \frac{\kappa_0^2}{(1 + \mu_0^2 St_0^2)(1 + \mu_1^2 (1 + M_0)^2 St_0^2)(1 + \mu_2^2 \kappa_0^2)}, \tag{8}$$

The free-stream velocity U_0 is selected as velocity scale while the chord length c and the maximum tip thickness d are chosen as characteristic length scales, respectively for the low- and high-frequency components.[14] The total tip noise spectra is then modeled by the sum of two uncorrelated spectral components related to different frequency domains using equation 8.

To account for changes in airplane angle of attack and flap deployment, Guo also provides an empirical geometry dependent correction factor (A_g, see equation 9) which modulates the spectral shape function derived above. In this equation, σ is the wing sweep angle, α the aircraft angle of attack and δ_F the flap deployment angle. A_0 is an absolute constant.

$$A_g = \begin{cases} A_0 (1 + \sin\sigma) \sin^2 \delta_F & \text{for low frequencies} \\ A_0 \frac{d}{c} (1 + \sin\sigma)(1 + \sin\alpha)^2 \sin^4(\alpha + \delta_F) & \text{for high frequencies} \end{cases} \tag{9}$$

Following Guo's[14] arguments, the total effect of flow Mach number variations is given by,

$$W(M_0) F(f, M_0) A_g = M_0^n \frac{F(f, M_0)}{I(M_0)} A_g, \tag{10}$$

where $I(M_0)$ is defined as the integral of the spectral shape function over a representative frequency range,

$$I(M_0) = \int_{f_1}^{f_2} F(f, M_0) df. \tag{11}$$

III. Experimental Approach

The data used for our present purpose originates from measurement campaigns performed in 2008 (see Rossignol[15] for more details regarding the experiment) and 2011 in DLR's Acoustic Wind Tunnel Braunschweig (AWB). Acoustic measurements done as part of DLR's project SLED (Silent Leading Edge Devices) are also available.[16] These measurements were performed in the Low Speed Wind Tunnel Braunschweig (NWB). In this set of experiments, measurements are performed at four different wind tunnel models. **(1)** An A320-type flap having a chord length of $c = 0.473$ m and a maximal thickness of $d = 0.065$ m (see figure 17a). In some cases, this first wing model was tested with a porous tip. The insert had a constant span of 0.02 m, or 5% of the full model span. It extends over 83% of the full chord length. **(2)** A high-lift wing model with a half-span flap of the same profile geometry as (1), but with a chord length of 0.12 m and a 0.4 m span (see figure 17b). **(3)** An aircraft half-model with deployed flaps and retracted slat (see figure 17c). **(4)** A cantilever wing with a DU-96 profile shape, having a chord length of 0.3 m and a span of 0.6 m (see figure 17d). Tests with the high-lift wing were done without slat deployment.

For each of these test models, an extensive investigation of acoustic emission characteristics was done. For the models instrumented with static pressure ports, pressure distributions on the model surfaces were also acquired. In selected test cases, and only for the A320-type flap wing, detailed flow measurements using the 7-hole probe technique were also made. The flow measurements were complemented by flow visualizations. Technical informations regarding the measurement techniques are given below. Measurements were done for Mach numbers ranging from $M_0 = 0.12$ to 0.18. The corresponding range of Reynolds numbers (based on the flap chord length) is given in table 1. Boundary layer tripping was not used on any of the models. For the type A320-type flap, this differs from previous experiments[15] where a square step was used to trip the boundary layers at $x/c = 0.01$ on the SS and $x/c = 0.34$ on the PS. This had no measurable impact on the tip flow field as well as on its acoustic emission.

Table 1: Flow parameters for the different test models cases. $c_0 = 343$ m/s, $\nu = 1.5 \times 10^{-5}$ m^2/s. Test case (3) is ommitted due to confidentiality issues.

U_0 [m/s]	M_0 [-]	(1), $Re_{c=0.473}$ [-]	(2), $Re_{c=0.12}$ [-]	(4), $Re_{c=0.3}$ [-]
40	0.12	1.26×10^6	0.32×10^6	0.80×10^6
50	0.15	1.58×10^6	0.40×10^6	1.00×10^6
60	0.18	1.89×10^6	0.48×10^6	1.20×10^6

A. Velocity Measurements

Flow field measurements were done only at the A320-type flap using a custom-build 7-hole probe. The probe was first traversed along the model SS and PS edges to quantify all three components of the mean velocity vector. The measurements were performed in the wind tunnel coordinate system defined in figure 2. In this figure the location of the probe is schematically given by the crosses (+) in the section cut view. The streamwise traverses have a resolution of $\approx 0.025c$, giving 42 measurement points per traverse. Furthermore, the mean flow field in chord-normal planes was acquired for a set of stations along the tip. The error on the measured velocity magnitude is estimated to be less than 1.0%.[17] This is valid provided that the flow angle, relative to the probe axis, does not exceed an angle of 70°. For larger angles, extensive flow separation occurs on the probe and makes it impossible to determine the correct velocity from the calibration charts. For the present case, the flow angle was found to exceed 70° relative to the probe axis in the proximity of the tip vortex core. For the remaining locations of interest, no particular difficulties occured. Spatial resolution was limited to 3 mm in both directions ($\Delta y = 3$ mm, $\Delta z = 3$ mm). The nearest measurement position relative to the model tip face was 8 mm and, relative to the model upper SS 5 mm. The size of the probe itself prfeatures from getting closer to the model. Due to the nearly 1 : 1 size of the isolated flap model, this resolution is sufficient in order to retrieve the important features of the mean flow around the tip. The stiffness of the probe was verified and its motion, due to an interaction with the highly 3D flow, was evaluated to be less than 1 mm, measured at the probe tip. Therefore, the accuracy of the probe position is estimated to be about ±1 mm.

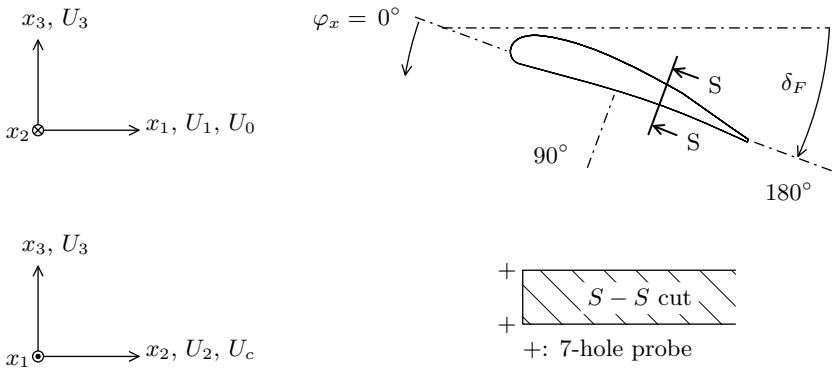

Figure 2: Definition of the coordinate system, the flap deployment angle (δ_F) and polar emission angle (φ_x). The crosses (+) shown in the section cut indicate the approximative position of the 7-hole probe when measuring the velocity near the tip edges.

B. Acoustic Measurements

In the AWB, sound source localization as well as quantification was performed using two different microphone arrays. A large aperture phased array with 96 1/2" Linear X M51 microphones and a smaller one having 48 1/4" Bruel & Kjær Type 4954 A microphones. Additionally, two far-field microphone were installed in the test section, outside the flow, to monitor background noise level variations between the different test setups. Data acquisition was done using two 48-channel GBM Viper measuring units. Data from all channels were simultaneously recorded at a maximal sampling rate of 65-kHz and with a 16 bit dynamic range. A total of 1228800 samples per microphone and datapoint was acquired. A 500-Hz high-pass and a 30-kHz anti-aliasing low-pass filter were set. Individual elements of the cross-spectral matrix, for the beamforming algorithm, for each data record were calculated by partitioning the time signals into 300 non-overlapping segments of 4096 samples. These segments were Fourier-transformed applying a rectangular window, yielding a frequency resolution of Δf = 15.87 Hz.

A view of the AWB experimental setups used during the acoustic measurements is given in figure 3a and 3b. Only the cantilever wing and the A320-type flap are shown. For these particular cases, noise measurements were performed using the small aperture phased array mounted on a traversing system. Although the sound directivity could be investigated using this approach, it is outside the scope of the present work. Attention is given only to noise radiated towards the ground (phased array looking at the models' PS). For the high-lift wing case, the model was installed horizontally between two acoustically lined side-walls, and noise measurements were done using the large aperture phased array located underneath it. The DU-96 wing originally had an aspect ratio of $AR = 2.67$ (0.8 m span, 0.3 m chord). It was, however, not possible to use the complete model span for the tests. The model had to be mounted vertically on a turntable as shown in figure 3b. A maximal aspect ratio of $AR = 2$ could be reached using this setup.

The experimental setup from the half-model tests in the NWB can be seen in figure 3c and 3d. The acoustic characterization of the test model was done through a large aperture microphone array as well as far field microphones. Integrated FSE noise spectra were obtained through integration of the array source maps in a small subregion including only the outboard FSE. Using the deconvolution algorithm CLEAN-SC,[18] FSE noise could be clearly identified and isolated.

IV. On the Spectrum of FSE Noise

In this section, the expression for the spectral shape of FSE noise (equation 8) and the geometrical correction factor (A_g) of equation 9 are used to represent existing experimental data. It will be shown that Guo's semi-empirical modelling approach provides a simple and versatile representation of noise generated at flap side-edges. However, while the effect of Mach number variations on the measured far-field noise levels can be properly predicted, the effect of flap deployment is not predicted accurately.

In figure 4, a plot of the measured far field acoustic spectra for the A320-type flap is presented. The reference (solid line) case is compared to a measurement made at a porous tip (dashed line). This comparison is made to define the usable frequency range of the measurements. In figure 4 both spectra were obtained with the small aperture phased array and a conventional beamforming algorithm. From

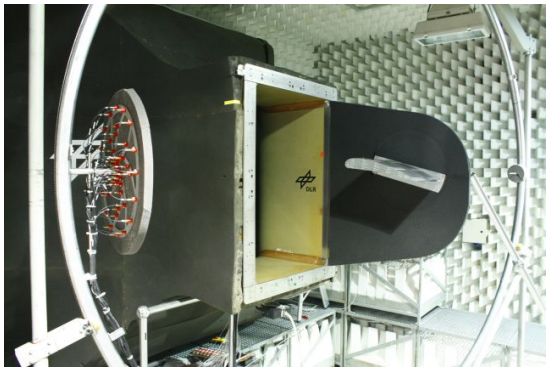

(a) A320-Type flap.

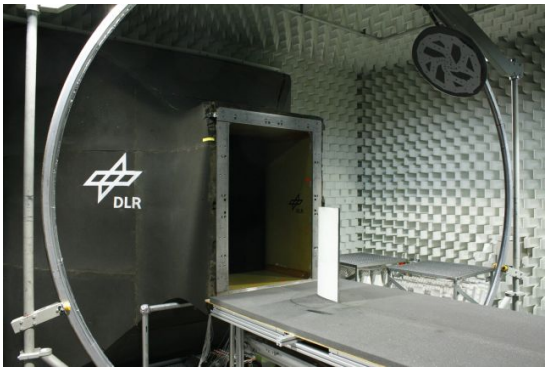

(b) DU-96 cantilever wing.

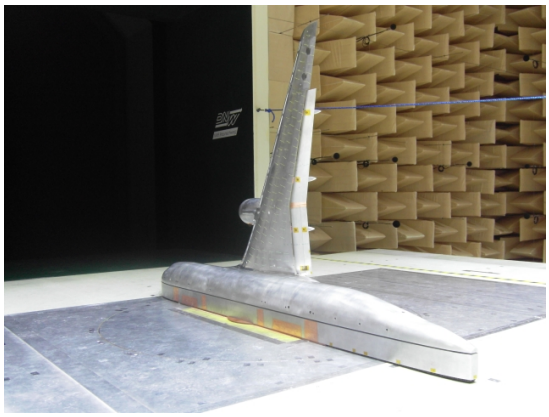

(c) Half-model in NWB.

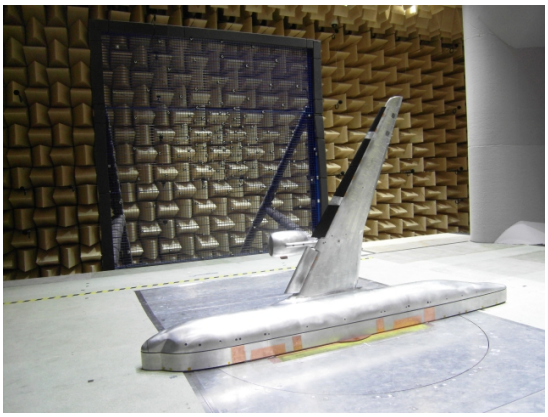

(d) Half-model in NWB.

Figure 3: Experimental setup for the acoustic measurements in the AWB and NWB.

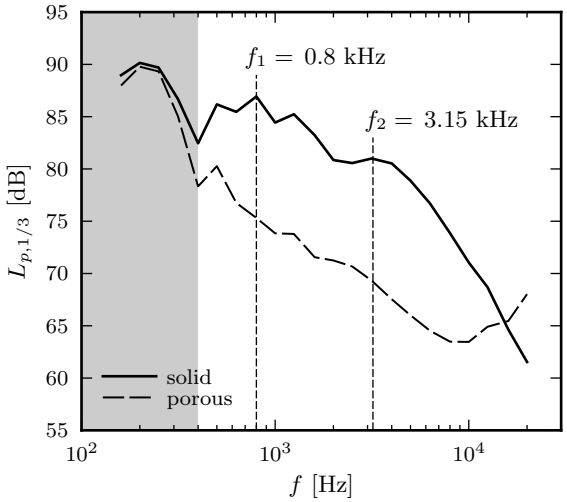

Figure 4: Comparison of the FSE noise spectra for a solid and a porous tip. $U_0 = 60$ m/s, $\delta_F = 30°$. Chordwise extent of the porous add-on is $0.83c$ for a spanwise extent of $0.05s$.

the array point-spread function, it is estimated that this microphone array has a sufficient resolution to isolate the tip noise source down to approximately 1.5 kHz. The comparison of figure 4 provides new insights in the data due to the large broadband noise reduction achieved when using the porous insert. Only a change in tip porosity was made, suggesting that only the tip noise source should be affected. Therefore, any noise reduction can be related to a reduction in FSE noise. This assumption is supported by experiments made by Storms and collaborators[13] who indicate no influence of a porous tip

on aerodynamic performance. Moreover, varying the integration regions used to analyse the microphone array data has practically no impact on the output spectra, as long as the tip is included in it. Spurious sources of noise therefore play a secondary role in defining the spectrum of figure 4. Consequently, in the range 0.4 kHz (3 dB offset between both curves) to 20 kHz, the measurement made at the A320-type flap are dominated by FSE noise.

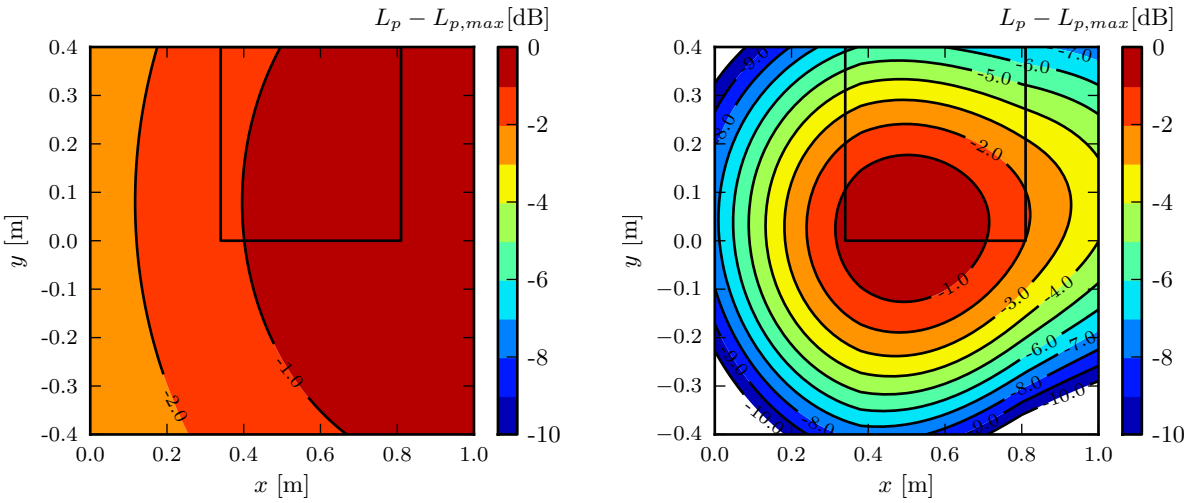

(a) $f = 0.8$ kHz **(b)** $f = 3.15$ kHz

Figure 5: Noise source maps. Relative sound pressure levels in dB (maximum = 0 dB). $U_0 = 60$ m/s, $\delta_F = 30°$. Phased array located underneath the A320-type flap model. Model represented by the black rectangle.

A double-hump structure in the spectrum clearly stands out, and two peak frequencies can be identified. The low-frequency peak occurs at $f_1 = 0.8$ kHz while the high frequency hump, reaches its maximum at $f_2 = 3.15$ kHz. These spectral features are related to different regions of the wing tip, as can be observed in the source maps shown in figure 5, for the same 1/3-octave band central frequencies. With the help of equation 3, the value of the constant μ_0 can now be set. Taking $c = 0.473$ m and $U_0 = 60$ m/s, one finds $\mu_0 = 0.15$ and $\mu_0 = 0.04$ for the low and high frequencies respectively. Therefore, the local length scales of interests are $l_0 = 0.04c$ and $l_0 = 0.15c$, for the high and low frequency spectral components respectively. Due to the lack of data for its evaluation the streamwise and spanwise coherence lengths are estimated to $l_1 = \mu_1 c = \mu_2 c$. In reality the spatial coherence length of the flow fluctuations should be larger in the streamwise direction than the spanwise direction. Table 2 provides an overview of the different parameters.

Table 2: Local length scales and constants used to model FSE noise according to Guo.[14]

	l_0 [m]	μ_0 [-]	μ_1 [-]	μ_2 [-]
low frequencies	$0.15c$	0.15	0.15	0.15
high frequencies	$0.04c$	0.04	0.04	0.04

Equations 8 and 9 are now applied, in conjunction with the parameters of table 2, to model the experimetal results (see figure 6). It is therefore implicitly assumed that the characteristic length scales of the flow structures responsible for the noise generation are independent of both Mach number and flap deployment angle. In figure 6a, measurement at $\delta_F = 25°$ and for three Mach numbers are presented. The plot of figure 6b shows the effect of flap deployment on the far field noise levels. In each of these plots the symbols stand for the experimental results and the lines are the corresponding semi-empirical representation. A constant factor K is used to calibrate the computed spectra on the exprimental results at $\delta_F = 25°$. The best fit of the measured data (in figure 6a) is obtained when assuming $p^2 \propto U^n$ with $n = 5.5$ and $n = 6.5$ for the low and high frequency components. In good agreement with Guo,[14] who proposes exponents of 5 and 6 respectively. While the impact of variations in Mach number is very well captured by the model, the dependency of the measured noise levels on flap deployment could be better represented (see figure 6b).

As already noted by Rossignol,[7] using local flow parameters to characterize FSE noise generation

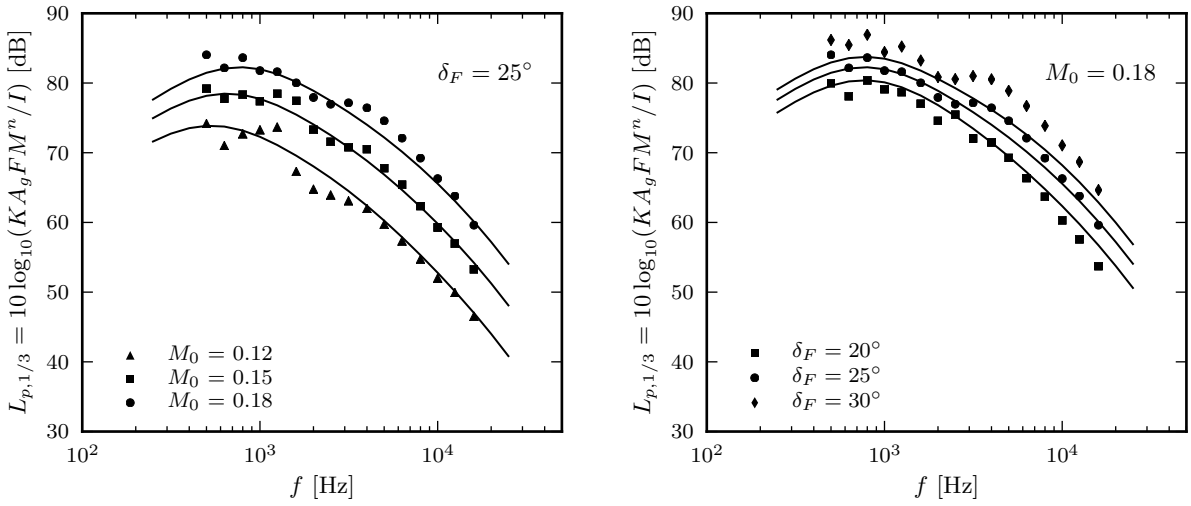

(a) Effect of Mach number.

(b) Effect of flap deployment.

Figure 6: Semi-empirical representation of measured FSE noise spectra according to equations 8 and 9. It is assumed that $p^2 \propto U^n$ with $n = 5.5$, 6.5 for the low and high frequency components. Model spectra calibrated on the $\delta_F = 25°$, $M_0 = 0.18$ case by adding a constant level offset (K).

could be a good approach to solve this issue. Although flow-based prediction methods can become computationally expensive, when relying on computational fluid dynamics (CFD), they are more flexible compared to geometry-based methods. This can be a real advantage when considering unconventional aircraft designs. The challenge for quick turnaround prediction methodologies based on flow characteristics is, therefore, to remain as flexible as possible while restricting the use of CFD to a minimum.

V. The FSE Flow Field and Noise Generation

The flow in the vinicity of the FSE is three-dimensional and highly turbulent. Noise is produced when the kinetic energy of turbulence is converted into acoustic energy by interacting with the FSE solid surfaces. The efficiency of this process is higher in the proximity of edges where the flow experiences a discontinuity.[19,20] It is therefore of prime interest to look at the flow near the flap tip edges. In this section, the results of the flow investigation are presented and discussed. The emphasis is put on the identification of distinctive flow features in the proximity of the tip edges which can be related to the noise production mechanism already discussed. Only the A320-type flap is considered for this part.

A. Velocity in the vicinity of the PS tip edge

The evolution of the mean flow velocity near the lower and upper tip edges is presented in figure 8 and 9 for three different deployment angles. In these plots, the velocity components have been normalized by the free-stream velocity, U_0. Looking first at figure 8, a striking first observation is the weak dependence of the U_1 and U_3 velocity components on δ_F. Increasing the flap deflection from 20° to 30° has, however, a strong impact on the second component (U_2). The larger the deployment angle, the larger must the spanwise flow deflection be. The chordwise evolution is first characterized by a sudden velocity increase at $x/c = 0.025$. This peak is related to the incoming flow being forced around the model's LE. The flow separates and is shed off as a shear layer with high spanwise velocity. This is a localized effect which does not show up in the U_3 component, where a progressive increase is observed until $x/c \approx 0.1$. After this first phase, the formation of the tip vortex begins under the action of the static pressure difference between the PS and SS. Between $x/c \approx 0.1$ and $x/c \approx 0.65$, the absolute value of both U_1 and U_3 maintain nearly constant values while U_2 grows in magnitude. The spanwise flow is accelerating and the tip vortex quickly gains in strength and size. Flow visualizations (see figure 7) clearly show the path taken by the tip face vortex, identified here as the primary vortex. It stays at the tip face up to a given chordwise station, dependent on flap deployment, before moving to the SS. In figure 8, this motion, and the subsequent lift-off from the SS surface, is accompanied by a decrease of all velocity components up to the TE.

The shear-layer induced contribution to the noise emission is directly related to the magnitude of the

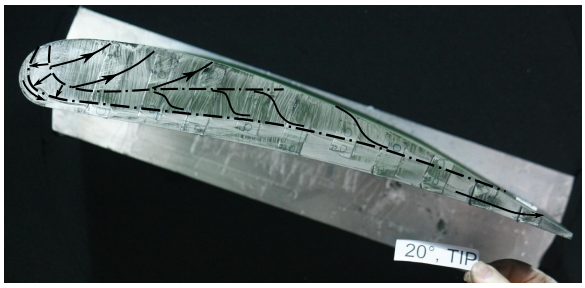

Figure 7: Flow visualization at the tip face, $\delta_F = 20°$. Approximative streaklines are sketched.

spanwise flow over the PS edge. For most of the chordwise extent, changing the flap deflection angle affects U_2 the most while U_1 and U_3 remain mostly unchanged for $x/c \leq 0.65$. Flap loading is therefore directly linked to the magnitude of the spanwise flow component. This observation is in agreement with Rossignol[15] who found that U_2 is a driving parameter for the noise production. The noise production mechanism exists over the whole tip extent. A natural choice of characteristic velocity scale for the shear-layer interaction mechanism is the magnitude of U_2 ($|U_2|$) near the PS tip edge at the x/c station, where it reaches its maximum value. This position is not constant and depends on δ_F. In the remaining of the text, this velocity scale will be refered to as U_c.

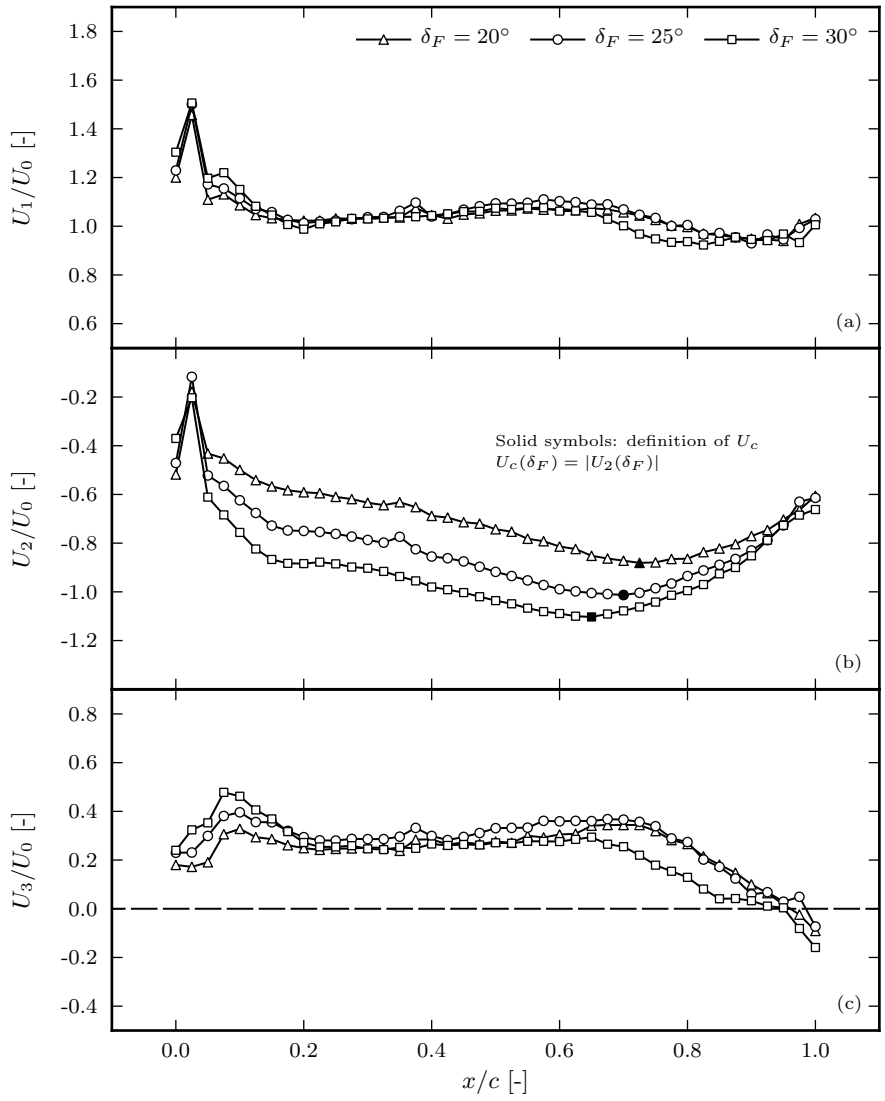

Figure 8: Streamwise evolution of the mean flow vector components at the PS edge. The solid symbols in (b) show the streamwise station used in defining the cross-flow velocity ($U_c(\delta_F) = |U_2(\delta_F)|$). U_c is dependent on δ_F and the position where it is picked moves upstream with an increase of δ_F.

B. Velocity in the vicinity of the SS tip edge

A quite different streamwise evolution of the velocity components is presented in figure 9 for the upper edge. Here again, strong velocity gradients between $x/c = 0.0$ and $x/c = 0.025$ are measured. This time, they are most important for the second and third components. As before, they are linked to the LE flow separation at the model tip. Downstream of $x/c = 0.025$ the first two components quickly reach a nearly constant level which is sustained up to $x/c \approx 0.4$ ($U_1/U_0 \approx 1.2$, $U_2/U_0 \approx 0.2$). At the same time, the normal velocity component (U_3) slowly grows up to $U_3/U_0 \approx 0.4$ between $0.2 < x/c < 0.35$ where a peak is reached. The chordwise position of the peak is dependent on the angle of attack.

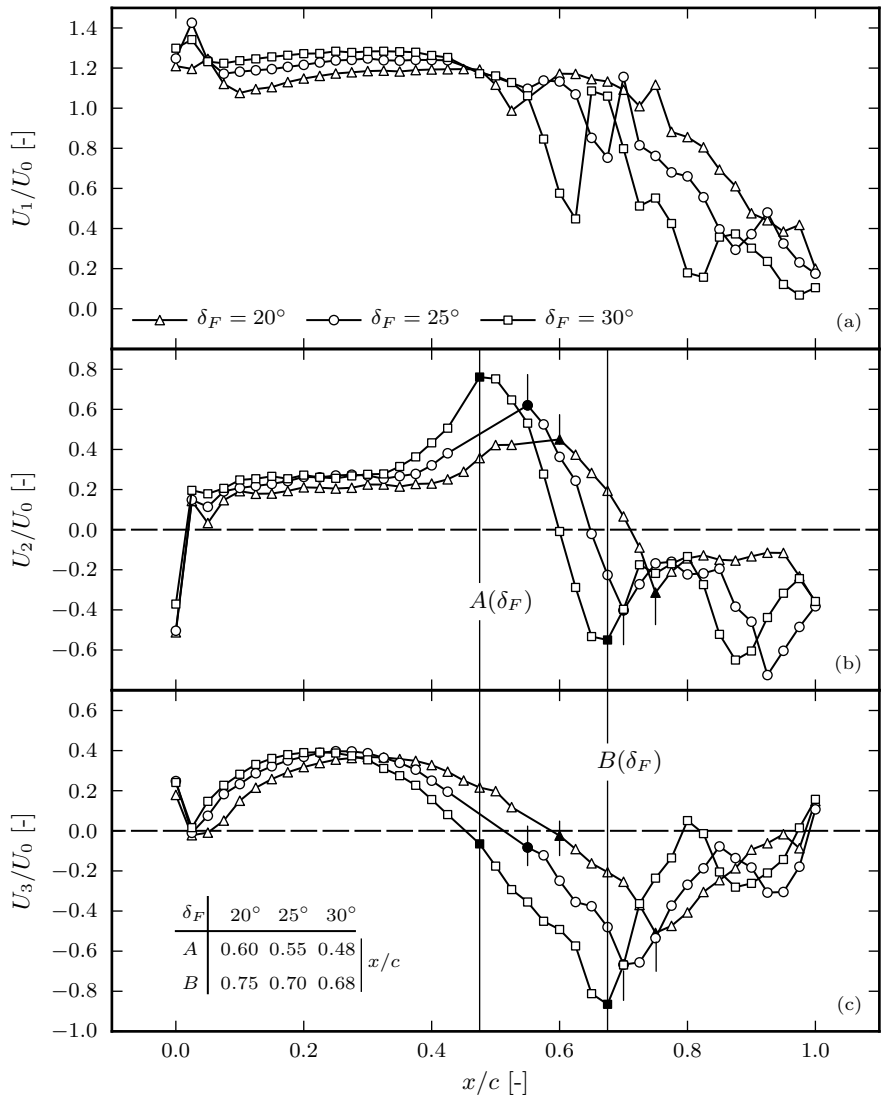

Figure 9: Streamwise evolution of the mean flow vector components at the SS (top) edge. The solid symbols in (b) and (c) show the streamwise position corresponding to station A and B. Both are dependent on δ_F and move downstream with a decrease of δ_F. Station A and B are defined according to the position of the first and second velocity peaks, downstream of $x/c = 0.4$, in (b).

The initial flow around the model LE is bend towards the wing's root, feeding the secondary vortex (or SS vortex). This holds between $x/c = 0.025$ and $x/c = 0.4$. At the latter position the primary vortex moves to the SS and merges with the secondary vortex. This could also be clearly seen in the flow visualizations (see figure 7). Starting at about $x/c \approx 0.35$ (depending on δ_F), the spanwise velocity component increases and quickly reaches a peak. For large δ_F, a higher velocity peak is reached further upstream than for small δ_F. The spanwise velocity component increase coincides with a decrease in normal and streamwise velocity; the flow is suddenly bent away from the tip. The subsequent ($0.5 \leq x/c \leq 0.8$) gradual variation in U_2 is related to the vortex core slightly moving toward the wing root before returning to the tip SS edge. This is confirmed by flow visualizations (not shown here). Further downstream, the spanwise velocity, U_2, quickly inverts to become negative. The primary vortex now

induces a negative spanwise velocity at the upper edge, with maximum magnitudes similar to those measured between $0.45 < x/c < 0.55$. The passage of the primary vortex to the SS also leads to a sign change of the U_3 velocity component. A minimum in U_3 is reached between $0.65 < x/c < 0.75$, its magnitude depending strongly on δ_F. At $\delta_F = 30°$ a peak value of $U_3/U_0 = 0.8$ is reached clearly showing the important downwash which occurs in the rear part of the wing tip. This minimum in U_3 coincides with a sudden and large increase in U_1 which is, however, not clearly understood. Further downstream, the magnitude of the streamwise component slowly decreases up to the TE, except for the occurence of a small hump at about $x/c \approx 0.85$ to $x/c \approx 0.95$. The magnitude of the spanwise and normal velocity components tend to oscillate up to the TE. These measured velocity humps could be related to a spiraling movement of the vortex core in the proximity of the upper edge. Corresponding results are shown in figure 10, however, additional investigations are required to confirm this assumption.

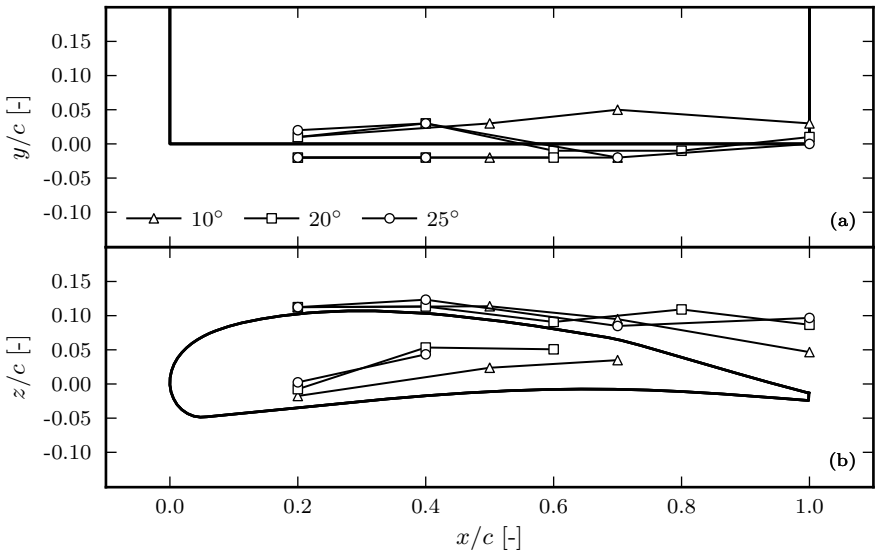

Figure 10: Measured vortex core paths. (a) Top view. (b) Side view.

As already discussed in the introduction, vortex-edge interactions in the aft half of the FSE result from streamwise instabilities of the tip vortex[9] and its proximity to the solid edge. After merging (station A, figure 9), the vortex is slightly bent away from the tip before crossing the uper tip edge a second time (at station B). It then lifts-off from the PS surface (around $x/c = 0.675$). The vortex cross-overs are always linked to local velocity increases. Station B is therefore considered to be at the center of the region where low frequency noise is generated. The magnitude of the cross-flow over the edge at station B is selected as characteristic velocity scale ($U_B = \sqrt{U_2^2 + U_3^2}$). Further, the flow measurements show that the vortex has grown to about $0.15c$, equivalent to the selected low-frequency values for $l_{0,1,2}$ in table 2. Therefore, the corresponding vortex-edge interaction, with $l_0 = 15c$, should lead to a low-frequency spectral contribution with a maximum at about $U/L \approx 0.8$ kHz. This is in perfect agreement with the experimental results of figure 4.

Vortex-edge interaction in the forward half of the FSE occurs when the primary vortex moves upwards and merges with the secondary vortex. In figure 9, merging happens at approximately $x/c = 0.475$ (it is, however, a function of δ_F). The merging process occurs at high velocities and noise is produced through interaction of unsteady vorticity fluctuations with the upper tip edge.[9,12,13,21] At station A, before merging, the vortex diameter is, from flow measurements, of about $0.03c$. The characteristic velocity of interest is once again the magnitude of the cross-flow near the SS edge ($U_A = \sqrt{U_2^2 + U_3^2}$). It is picked out at station A in figure 9. With this, the frequency of the dominant flow structures is of order $U/L \approx 3.3$ kHz. Also in accordance with the observation of figure 4. Each of the above mechanisms is characterized by a length and a velocity scale. Their value is directly extracted from flow measurements in normal planes along the model chord (not shown here). Hereby, the vortex diameter, characterized by L, is taken as a constant and only U is allowed to change for changes in δ_F. This is justified by the fact that the chordwise station at which the flow features where the noise production takes place moves upstream with flap deployment.

The above observations, supplemented by results from the relevant literature of section I, suggest that the total spectrum of FSE noise is the sum of four uncorrelated contributions originating from flow-edge interactions at the flap tip. In order of importance,

1. Vortex-edge interaction in the aft half.
2. Vortex-edge interaction with the SS edge during vortex merging.
3. Shear-layer instabilities over the whole of the PS edge.
4. Vortex-edge interaction near the tip TE at low flap deflection angles.

Only the first two contributions are considered in the subsequent modelling. The remaining contributions are not further investigated because they are unlikely to occur in practice for standard high-lift configurations.

VI. An Adapted Representation of the FSE Noise Spectra

The evolution of the characteristic velocity scales at station A and B (variable x/c) as well as of U_c (also variable x/c) is plotted in figure 11 as a function of flap deployment. A linear relationship between the velocity scales and the flap angle is assumed as follows:

$$\frac{U_c}{U_0} = 0.023\delta_F + 0.415 \qquad \text{PS cross-flow,} \tag{12}$$

$$\frac{U_A}{U_0} = \frac{\sqrt{U_2^2 + U_3^2}}{U_0} = 0.042\delta_F - 0.456 \qquad \text{SS cross-flow at station A,} \tag{13}$$

$$\frac{U_B}{U_0} = \frac{\sqrt{U_2^2 + U_3^2}}{U_0} = 0.052\delta_F - 0.524 \qquad \text{SS cross-flow at station B.} \tag{14}$$

Four hypotheses are made before formulating an adapted model of FSE noise based on equation 8.

1. Noise production is driven by the flap loading. Its expression is the spanwise flow magnitude at the PS edge, which includes effects of changes in free-stream velocity and flap deployment
2. Radiated noise intensity is proportional to the cross-flow velocity to the n^{th} power of U_c. ($I \propto U_c^n$).
3. The total tip noise spectrum is due to the summed contribution of two independent spectral components i.e. vortex-edge interaction in the aft half and with the SS edge during vortex merging.
4. The relevant length scale, for the aeroacoustic problem, is independent of flap loading ($l_0 \neq \mathcal{F}(C_L)$).

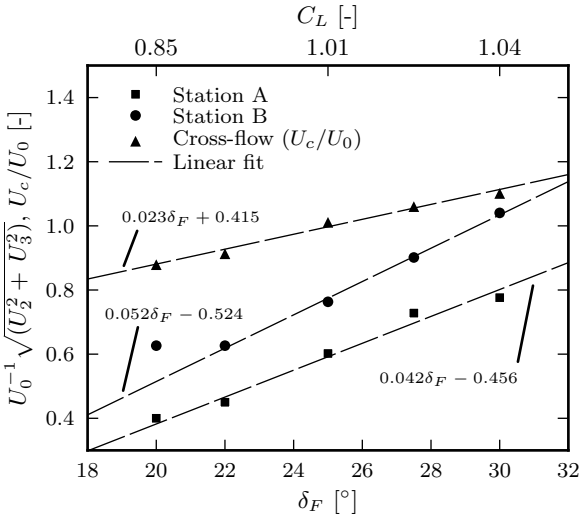

Figure 11: Characteristic velocity scales.

As was done in section IV, the constants of equation 8 ($\mu_{0,1,2}$) are set based on the spectra of figure 4 for the solid case and the velocity scales according to equations 12 to 14 (see also figure 11). Hereby, the linear relationships in figure 11 at stations A and B are used to get the peak frequencies of both spectral components for any desired combinations of flow conditions and flap deployment. Instead of using global Strouhal (St_0) and Mach numbers (M_0) in equation 8 we define local quantities based on the parameters given above.

$$St_{loc} = \frac{f l_{loc}}{U_{loc}}, \quad M_{loc} = \frac{U_{loc}}{c_0}, \tag{15}$$

with $l_0 = 0.164c$ and $U_{loc} = U_B$ for the low-frequency component and $l_0 = 0.032c$ and $U_{loc} = U_A$ for the high-frequency components. See table 3 for an overview of the adapted model parameters. The values for l_0 differs from those of table 2 due to the use of new characteristic velocitity scales (equations 13 to 14) for its derivation using equation 3 and the components peak frequencies identified in figure 4. The adapted spectral shape function becomes,

$$F = \frac{\kappa_0^2}{(1+\mu_0^2 St_{loc}^2)(1+\mu_1^2(1+M_{loc})^2 St_{loc}^2)(1+\mu_2^2\kappa_0^2)}, \tag{16}$$

with $\mu_{0,1,2} = 0.164$ for low-frequency component and $\mu_{0,1,2} = 0.032$ for the high-frequency component. Following Guo's[14] arguments, the total effect of flow Mach number variations is given by,

$$W(M_c)F(f, M_{loc}) = M_c^n \frac{F(f, M_{loc})}{I(M_{loc})}, \tag{17}$$

where $I(M_{loc})$ is defined as the integral of the spectral shape function over a representative frequency range, i.e.

$$I(M_{loc}) = \int_{f_1}^{f_2} F(f, M_{loc}) df. \tag{18}$$

Equation 18 expresses the overall contribution of the spectral shape function to the FSE noise levels. The local interaction of the turbulent flow with the solid edges is reponsible for noise generation and, therefore, defines its spectral shape. This is why only local flow parameters (identified in the previous section) enter the formulation of equation 16. The implicit dependency of F on Mach number variations is normalized out by equation 18. The advantage of using the PS cross-flow velocity, U_c, as scaling parameter lies in its ability to account for flap deployment. Therefore, the purely empirical correction factors A_g (equation 9) are not needed.

Table 3: Local length scales and constants used to model FSE according to the adapted formulation.

	l_0 [m]	μ_0 [-]	μ_1 [-]	μ_2 [-]
low frequencies	$0.164c$	0.164	0.164	0.164
high frequencies	$0.032c$	0.032	0.032	0.032

Typical High-Lift Profile Geometries FSE Noise Examples

The modeled total noise spectra, computed according to equations 16 and 17, are plotted in figure 12 for the A320-type flap. In this figure, the produced spectra were calibrated (by adding a level offset) to get the best possible representation of the measured data at $\delta_F = 30°$ and $U_0 = 60$ m/s. The predictions of figure 12 assume velocity scaling exponents of $n = 5.5$ and $n = 6.5$, for the low- and high-frequency spectral components respectively.

Of course, when considering quick turnaround noise prediction methodology, it is critical to provide a semi-empirical model which is as flexible as possible. To evaluate this aspect, the formulation used to produce the prediction in figure 12 is directly applied to further experimental databases. For the following case, the calibration of figure 12 is retained. Acoustic measurement made at a high-lift wing with an half-span flap (as described in section III) serve as a first test. The computed FSE noise spectra (lines) are presented in figure 13 along with the experimental data (solid symbols). A second test is performed using the SLED database for the half-model (test case (3)). It is shown in figure 14. To achieve such a good agreement between experiment and prediction, an effective flap deployment angle (δ_F') has to be considered and used in equations 12 to 14. The effective δ_F obtained in this way are solely defined based on a good agreement between measurement and predicion. This procedure is, however, justified by the different model geometries and configurations which have different aerodynamic characterisitcs. FSE noise is related to the flap loading and, therefore, for similar geometries, equal noise levels should be generated at equal loading (C_L). The validity of the effective deployment angles needed to bring together the acoustic measurements and predictions is checked by comparing each models' C_L for the cases plotted in figures 12 to 14. The comparison is shown in figure 15. Except for the DU96 wing, all C_Ls were computed from either CFD or pressure measurements. For the DU96 wing, estimated C_Ls are obtained through interpolation of the A320-type flap polar at the corresponding δ_F'. Although, the δ_F' determined in this way do not exactly match those above, an acceptable agreement is found, thus confirming the trends of figures 12 to 14. In practice, knowledge of the C_L for the case of interest would, therefore, suffice to derive all the parameters needed to predict the far field noise levels.

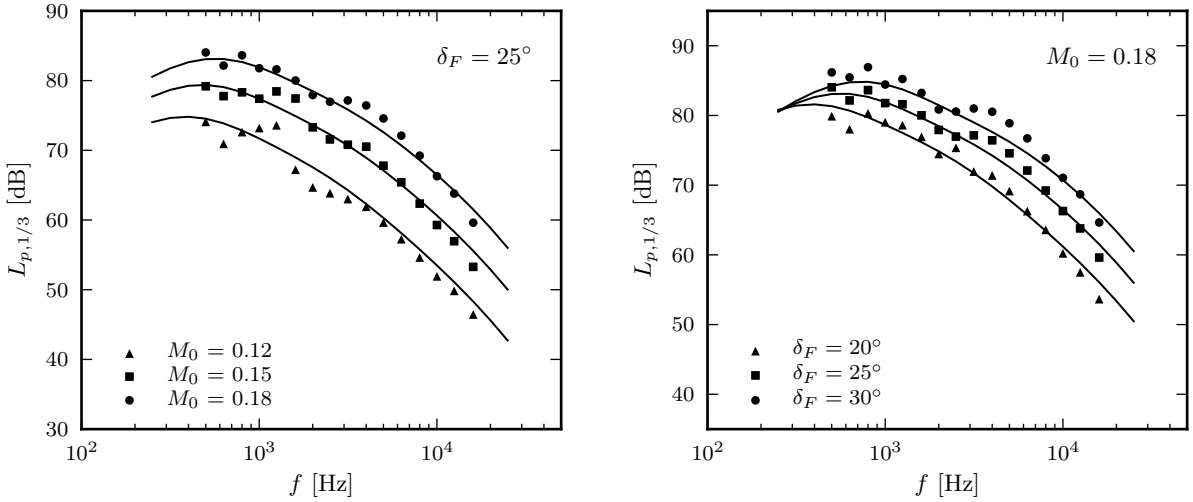

(a) Mach number effect.

(b) Flap deflection effect.

Figure 12: A320-type flap model FSE noise. Prediction of the effect of Mach number variations assuming $p^2 \propto U_c^n$ with $n = 5.5, 6.5$ for the low-frequency and high-frequency contributions. Solid symbols: measurements. Lines: prediction.

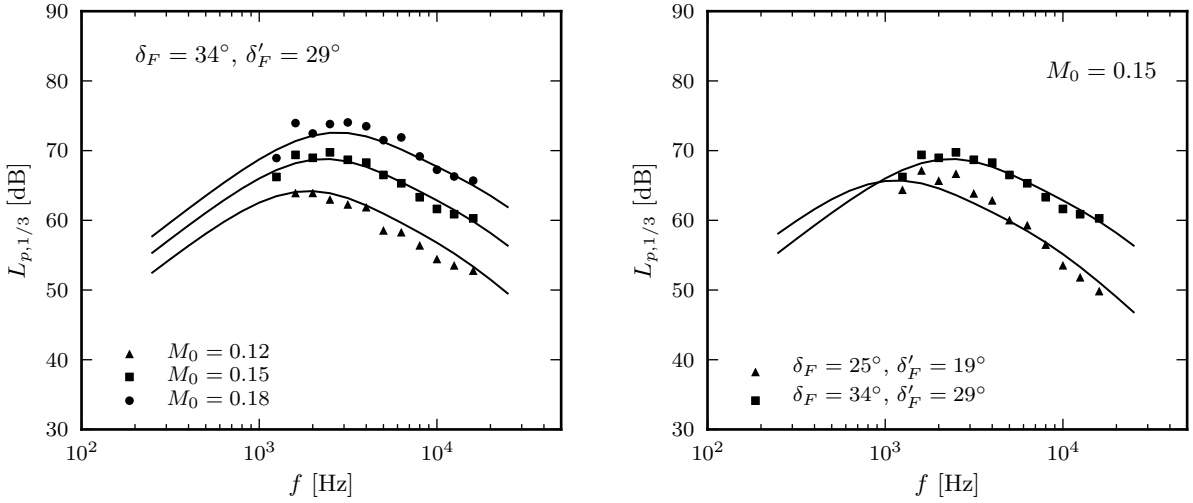

(a) Mach number effect.

(b) Flap deflection effect.

Figure 13: High-lift wing model FSE noise. Prediction of the effect of Mach number variations assuming $p^2 \propto U_c^n$ with $n = 5.5, 6.5$ for the low-frequency and high-frequency contributions. Solid symbols: measurements. Lines: prediction.

Non-Typical Profile Geometries FSE Noise Example

A similar exercise is made with experimental acoustic data from the DU-96 cantilever wing. See section III for more details about this model. Here again, it is necessary to consider an effective angle of attack to achieve the good agreement between prediction and experiment which is shown in figure 16. Furthermore, the characteristic length scales of the flow structures reponsible for the noise generation ($l_{0,1,2}$) also need to be adjusted. Hereby, from the measurements, the low frequency peak is found at about $f = 1.2$ kHz and the high frequency peak is found at approximately $f = 4$ kHz. Using equation 3 coupled with equations 12 to 14 one can obtain the adjusted constants of equation 16. Namely, for the low frequency component $\mu_{0,1,2} = 0.069c$ and for the high frequency component $\mu_{0,1,2} = 0.015c$. This choice, however, needs experimental validation by flow field measurements or CFD.

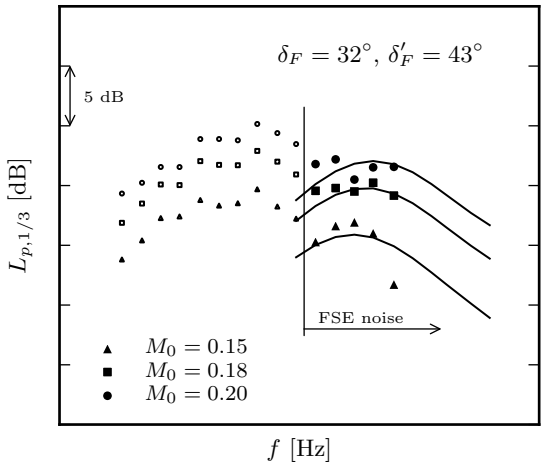

Figure 14: Half-model FSE noise. Same methodology as in figures 12 and 13. Solid symbols: measurements. Lines: prediction.

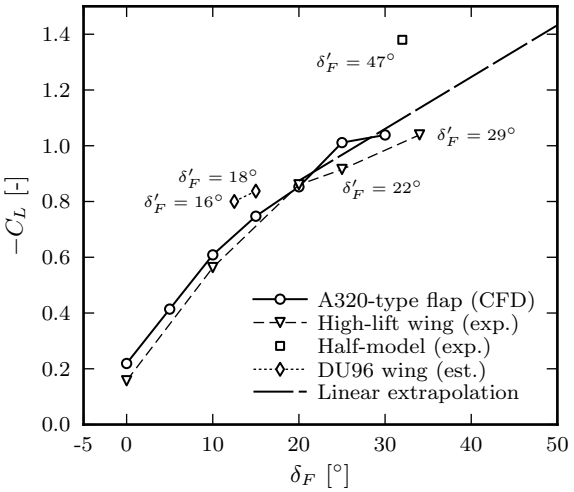

Figure 15: Flap sectional lift coefficient ($-C_L$) versus flap deployment. Comparison between estimated (est.), experimental (exp.) and computed values (CFD).

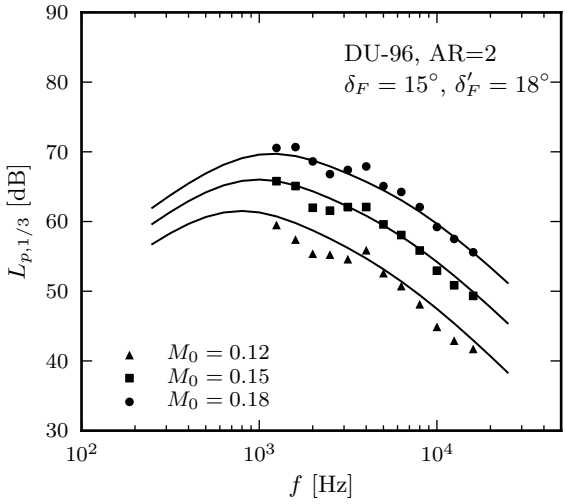

(a) Mach number effect.

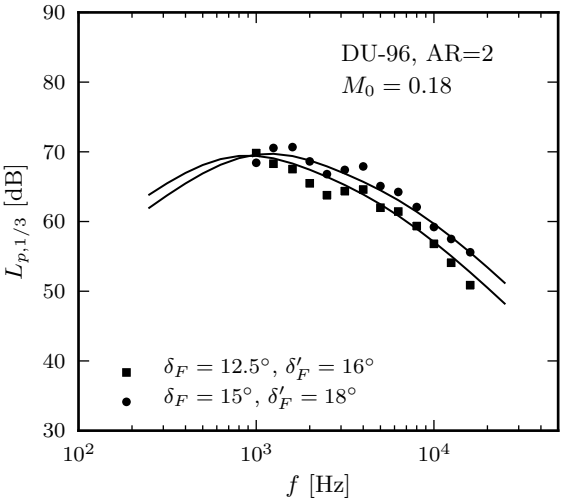

(b) Flap deflection effect.

Figure 16: DU-96 cantilever wing tip noise. Prediction of the effect of Mach number variations assuming $p^2 \propto U_c^n$ with $n = 5.5, 6.5$ for the low-frequency and high-frequency contributions. Solid symbols: measurements. Lines: prediction.

Unresolved Issues

From the preceding discussion it appears that two important aspects still need to be resolved. **(1)** A crude approximation was first made by assuming the invariability of the characteristic length scale of the flow structures responsible for the noise production. This assumption was justified by the variable chordwise location at which the tip vortex size is evaluated. Larger flap deflection resulting in higher velocities and a shorter development length for the vortex. Although this assumption appears appropriate between similar geometries of different chord lengths, changing the tip profile geometry appears to have an important impact on the chracteristic dimensions of the flow structures. This is an unresolved issue which will require further analysis of the tip vortex flow dynamics. **(2)** When comparing noise radiation from different test configurations, an effective flap deflection angle has to be used to achieve a good agreement of the predicted FSE noise spectra with the measured acoustic data. This angle does not, however, correspond to the free-stream (or flight) flap deployment. It merely puts the configurations on

a similar basis with the refence A320-type flap. An evaluation of this correction is beyond the scope of the present work and is left to future research efforts.

VII. Conclusion

A modeling approach for FSE noise is presented which is based on characteristics of the flow field in the vicinity of wing tip edges. Detailed flow measurements are performed to isolate distinct features related to the most important sources of aeroacoustic noise. Along the lines of Guo,[14] the proposed scheme assumes the total FSE noise spectrum to be the summed contributions due to two independent source mechanisms. Unsteady vorticity fluctuations, originating from the PS shear layer, sweeping over the forward half of the upper tip edge at high velocities, lead to mid-to-high frequency noise production. Vortex interaction with the SS surface near the flap tip aft half, after vorex merging, are assumed to be the main contributor in the low-to-mid frequency range.

From the flow measurements, the characteristic length and velocity scales of both mechanisms are quantified. The spectral shape of each contributor to the total FSE noise is represented according to Guo's formulation[14] adapted to the identified local parameters. Because the proposed velocity scales are dependent on flap deployment, an accurate prediction of both Mach number and flap angle effects is achieved. There is no need for an additional correction factor, as proposed by Guo.[14] It is also found that this new formulation provides a very good representation of FSE noise over a large range of wing configurations. Ranging from a single isolated cantilever wing to a complex half-model with a conventional high-lift wing. For specific applications, the parameters needed as input to the prediction scheme could also be easily extracted from CFD computations.

Although the prediction scheme has a wide range of applicability it seems, however, that the wing tip geometry plays an important role, greatly influencing noise production. This aspect is not covered in the present work and will require more research efforts. Furthermore, an extrapolation of the results to full-scale remains out of the scope of this paper and is left to future work.

Acknowledgements

The author would like to gratefully thank Dr. Johann Reichenberger from EADS-IW for providing the porous flap tip and Dr. Roger Drobietz from GE Wind Energy for providing the DU-96 wing model. Also, many thanks to Dr. Jochen Wild and Michael Pott-Pollenske for making the SLED database available.

References

[1]Hardin, J. C., "Noise generation at the side edges of flaps," *AIAA Journal*, Vol. 18, No. 5, 1980, pp. 549–552.

[2]Howe, M. S., "On the generation of side-edge flap noise," *Journal of Sound and Vibration*, Vol. 80, No. 4, Feb. 1982, pp. 555–573.

[3]Sen, R., "Local dynamics and acoustics in a simple 2D model of airfoil lateral-edge noise," *2nd AIAA/CEAS Aeroacoustics Conference*, 1996.

[4]Guo, Y., "Prediction of flap side edge noise," *AIAA Journal*, Vol. 1, 1999, pp. 35–45.

[5]Brooks, T. and Marcolini, M., "Airfoil Tip Vortex Formation Noise," *AIAA Journal*, Vol. 24, No. 2, 1986, pp. 246–252.

[6]Guo, Y. and Yamamoto, K., "Component-Based Empirical Model for High-Lift System Noise Prediction," *Journal of Aircraft*, Vol. 40, No. 5, 2003, pp. 914–922.

[7]Rossignol, K.-S., "Empirical Prediction of Flap Tip Noise," *Proceedings of the 17th AIAA/CEAS Aeroacoustics Conference, Portland, Oregon*, No. AIAA 2011-2733, June 2011.

[8]Batchelor, G., *An Introduction to Fluid Dynamics*, Cambridge University Press, 1967.

[9]Streett, C., "Numerical Simulation of Fluctuations Leading to Noise in a Flap-Edge Flowfield," *36th Aerospace Sciences Meeting and Exhibit*, 1998.

[10]Choudhari, M. M., Lockard, D. P., Macaraeg, M. G., Singer, B. A., Streett, C. L., Neubert, G. R., Stoker, R. W., Underbrink, J. R., Berkman, M. E., and Khorrami, Mehdi R., e. a., "Aeroacoustic Experiments in the NASA Langley Low-Turbulence Pressure Tunnel," Tech. Rep. L-18131; NASA/TM-2002-211432, Langley Research Center, February 2002.

[11]Brooks, T. and Humphreys Jr., W. M., "Flap Edge Aeroacoustic Measurements and Prediction," *6th AIAA/CEAS Aeroacoustics Conference*, 2000.

[12]Guo, Y., Joshi, M., Bent, P., and Yamamoto, K., "Surface Pressure Fluctuations on Aircraft Flaps and their Correlation with Far-Field Noise," *Journal of fluid mechanics*, Vol. 415, 2000, pp. 175–202.

[13]Storms, B. L., Ross, J. C., Horne, C. W., Hayes, J. A., Dougherty, R. P., Underbrink, J. R., Scharpf, D. F., and Moriarty, P. J., "An Aeroacoustic Study of an Unswept Wing with a Three-Dimensional High-Lift System," Tech. Rep. NASA/TM-1998-112222, NASA, February 1998.

[14]Guo, Y., "Aircraft Flap Side Edge Noise Modeling and Prediction," *Proceedings of the 17th AIAA/CEAS Aeroacoustic Conference, Portland, Oregon*, No. AIAA 2011-2731, June 2011.

[15]Rossignol, K.-S., "Development of an Empirical Prediction Model for Flap Side-Edge Noise," *Proceedings of the 16th AIAA/CEAS Aeroacoustics Conference, Stockholm, Sweden*, No. AIAA 2010-3836, June 2010.

[16]Kühn, T., "Aerodynamische Vermessung lärmarmer Hochauftriebssysteme im Rahmen des DLR-Projekts SLED," Tech. Rep. IB 124-2013/908, DLR, 2013.

[17]Zilliac, G. G., "Modeling, calibration, and error analysis of seven-hole pressure probes," *Experiments in Fluids*, Vol. 14, No. 1, Dec. 1993, pp. 104–120.

[18]Sijtsma, P., "CLEAN Based on Spatial Source Coherence," *13th AIAA/CEAS Aeroacoustics Conference (28th AIAA Aeroacoustics Conference) , Rome, Italy*, No. AIAA-2007-3436, May 2007.

[19]Williams, J. E. F. and Hawkings, D. L., "Sound Generation by Turbulence and Surfaces in Arbitrary Motion," *Philosophical Transactions of the Royal Society of London. Series A, Mathematical and Physical Sciences (1934-1990)*, Vol. 264, No. 1151, May 1969, pp. 321–342.

[20]Williams, J. E. F. and Hall, L. H., "Aerodynamic sound generation by turbulent flow in the vicinity of a scattering half plane," *Journal of Fluid Mechanics Digital Archive*, Vol. 40, No. 4, 1970, pp. 657–670.

[21]Koop, L., *Aktive und Passive Strömungsbeeinflussung zur Reduzierung der Schallabstrahlung an Hinterkantenklappen von Tragflügeln.*, Ph.D. thesis, Technische Universität Berlin, 2005.

Appendix A : Wind Tunnel Models Geometries

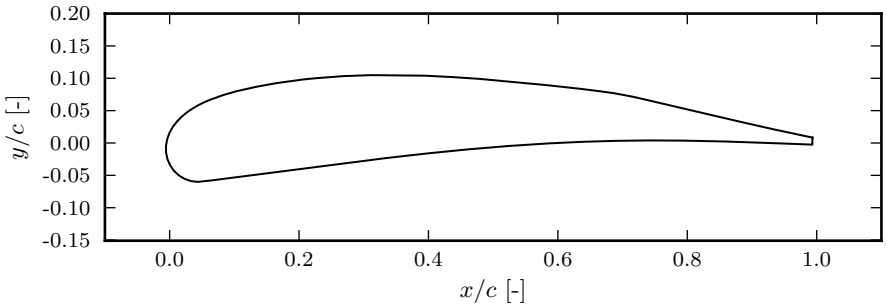

(a) A320-type flap. c = 0.473 m.

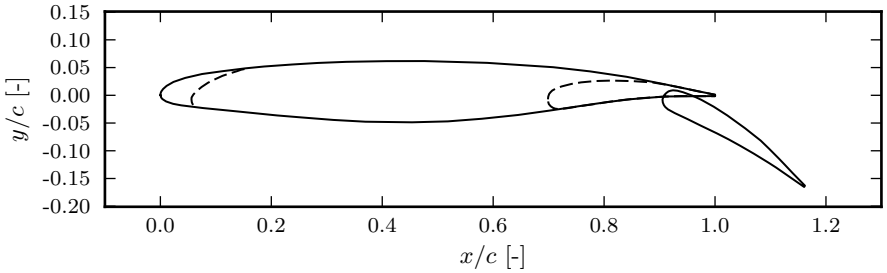

(b) High-lift wing model. c = 0.4 m.

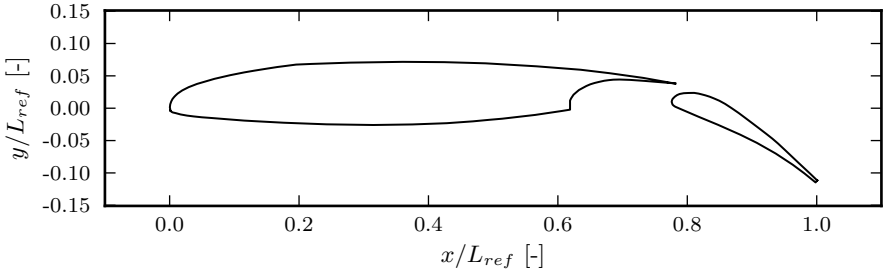

(c) Aircraft half-model wing section. L_{ref} = arbitrary length scale.

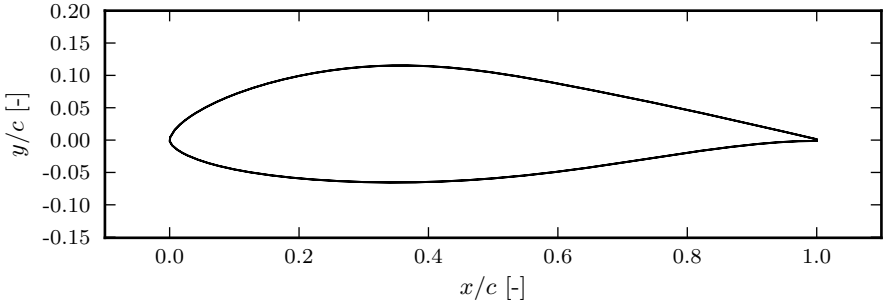

(d) DU-96 cantilever wing. c = 0.3 m.

Figure 17: Geometry of the tested wing models.